Title	Nonlinear behavior of resistive pressure driven modes in stellarator/heliotron plasmas with vacuum magnetic islands
Author(s)	Unemura, T.; Hamaguchi, S.; Wakatani, M.
Citation	Physics of Plasmas. 2004, 11(4), p. 1545-1551
Version Type	VoR
URL	https://hdl.handle.net/11094/78488
rights	This article may be downloaded for personal use only. Any other use requires prior permission of the author and AIP Publishing. This article appeared in Physics of Plasmas 11, 1545 (2004) and may be found at https://doi.org/10.1063/1.1688335.
Note	

Nonlinear behavior of resistive pressure driven modes in stellarator/heliotron plasmas with vacuum magnetic islands

T. Unemura, S. Hamaguchi, and M. Wakatani

View Online   Export Citation

Nonlinear behavior of resistive pressure driven modes in stellarator/heliotron plasmas with vacuum magnetic islands

T. Unemura,[a] S. Hamaguchi, and M. Wakatani[b]

Graduate School of Energy Science, Kyoto University, Gokasyo, Uji, Japan 611-0011

Effects of externally applied vacuum magnetic islands (VMIs) on nonlinear saturation levels of resistive pressure driven modes in stellarator/heliotron plasmas are examined with the use of three-dimensional nonlinear time-evolution simulations for cylindrical plasmas. The simulation code is based on reduced magnetohydrodynamics equations and the equations are discretized by the finite element method in the poloidal cross section and Fourier expansion in the toroidal direction. It is shown that the growth of magnetic islands in a plasma can be controlled by an external perturbational magnetic field that generates VMIs. © *2004 American Institute of Physics.* [DOI: 10.1063/1.1688335]

I. INTRODUCTION

Resistive pressure driven (i.e., interchange) instabilities are known to induce the formation of magnetic islands.[1–3] Presence of such magnetic islands can adversely affect the stability and transport of currentless plasmas confined in stellarator/heliotron devices.[4–9] To date many experimental and theoretical studies have been devoted to examining effects of magnetic islands on plasma profiles and instabilities. For example, externally generated magnetic islands, which we call vacuum magnetic islands (VMIs), were applied to helical plasmas to control the growth of magnetic islands in the Large Helical Device (LHD).[10,11]

In this paper, we use numerical simulations to examine effects of VMIs on the growth of magnetic islands driven by resistive pressure driven instabilities in stellarator/heliotron plasmas. The governing nonlinear equations we use are the reduced magnetohydrodynamics (RMHD) equations[12,13] in cylindrical coordinates with pressure profiles unstable to resistive pressure driven modes. The discretization scheme used in the numerical code is the finite element method (FEM) in the poloidal cross section, which in general allows us to calculate plasmas with an arbitrary poloidal cross sectional shape. In this work, however, we only present simulation results for plasmas with circular cross sections for the sake of simplicity.

The rest of the paper is organized as follows: In Sec. II, the model equations are given and the numerical method used in our simulation code is discussed briefly. The simulation parameters are given in Sec. III and simulation results are presented in detail in Sec. IV. In Sec. V we draw conclusions.

II. MODEL EQUATIONS AND THE NUMERICAL METHOD

We use the following RMHD equations[12,13] to examine nonlinear resistive pressure driven modes in a straight stellarator/heliotron plasma:

$$\frac{\partial \omega}{\partial t} = [\phi, \omega] + [\nabla_\perp^2 A, \psi] + \frac{\partial}{\partial \zeta} \nabla_\perp^2 A + [\Omega, p] + \mu \nabla_\perp^2 \omega, \tag{1}$$

$$\frac{\partial A}{\partial t} = [\phi, \psi] + \frac{\partial \phi}{\partial \zeta} + \eta_\parallel \nabla_\perp^2 A, \tag{2}$$

$$\frac{\partial p}{\partial t} = [\phi, p] + \chi_\parallel \nabla_\parallel^2 p + \chi_\perp \nabla_\perp^2 p, \tag{3}$$

$$\omega = \nabla_\perp^2 \phi, \tag{4}$$

$$\psi = A + \psi_h, \tag{5}$$

where dependent variables are the electrostatic potential ϕ, poloidal flux A, and plasma pressure p. The total poloidal flux ψ is defined as the sum of A and the average poloidal flux ψ_h generated by the external stellarator/heliotron field coil currents. Equation (4) defines the vorticity ω. The function Ω denotes the average curvature of helical magnetic field which is defined by Eq. (7) below under cylindrical symmetry. The collisional diffusion parameters are the viscosity μ, the plasma resistivity $\eta_\parallel$, and the thermal diffusivities in the parallel and perpendicular directions, $\chi_\parallel$ and $\chi_\perp$.

Let us consider a cylindrical plasma and use the ordinary cylindrical coordinates (r, θ, ζ). We denote the minor and major radii of the plasma by a and R_0 and the toroidal magnetic field (i.e., magnetic field in the ζ direction) by B_0. The length of the cylinder is then given by $2\pi R_0$ and the inverse aspect ratio by $\epsilon \equiv a/R_0$. The stellarator/heliotron field ψ_h and the average curvature Ω depend on r only and are related to the rotational transform $\iota(r)$ through

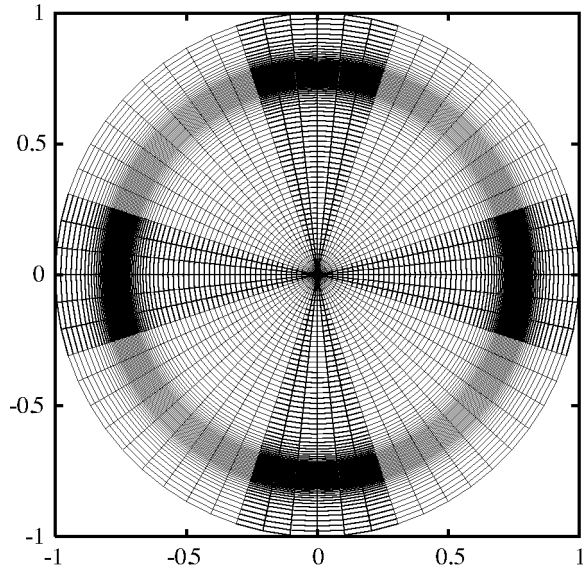$$\iota(r) = -\frac{1}{r} \frac{d\psi_h}{dr} \tag{6}$$

FIG. 1. Typical FEM grids in the poloidal cross section used for the simulations presented in this work. The length is scaled by the minor radius.

and

$$\Omega(r) = \frac{N\epsilon^2}{l}\left(r^2\iota(r) + 2\int_0^r r\iota(r)dr\right) \tag{7}$$

for a stellarator/heliotron device with the pole number l and the period number N.[14] The Poisson bracket [ ] is defined as $[f,g] \equiv (\hat{\zeta} \times \nabla f)\cdot\nabla g$.

All variables in Eqs. (1)–(5) are dimensionless and these variables may be converted to the dimensional ones via

$$t = \frac{a}{\epsilon v_A}t, \quad r = ar, \quad \zeta = R_0\zeta,$$

$$J_\parallel = \frac{\epsilon B_0}{\mu_0 a}J_\parallel, \quad \phi_e = \epsilon a v_A B_0\phi, \quad \psi_h = \epsilon a B_0\psi_h,$$

$$\Omega = \epsilon\Omega, \quad p = \frac{\epsilon B_0^2}{\mu_0}p, \quad A = \epsilon a B_0 A,$$

$$\eta_\parallel = \mu_0\epsilon a v_A\eta_\parallel, \quad \mu = \epsilon a v_A\mu,$$

$$\chi_\perp = \epsilon a v_A\chi_\perp, \quad \chi_\parallel = \epsilon a v_A\chi_\parallel,$$
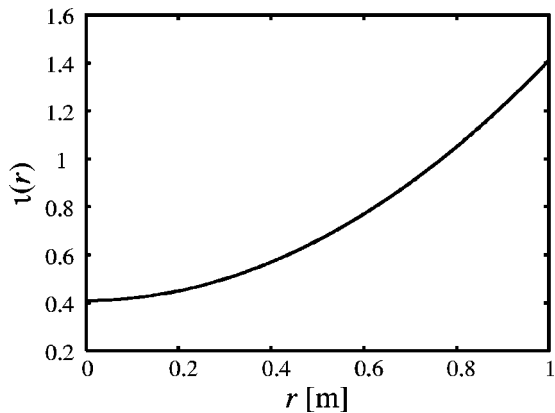

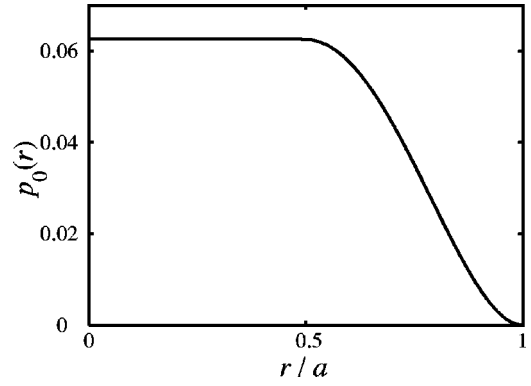FIG. 2. The rotational transform used in the simulations.

FIG. 3. The equilibrium plasma pressure profile used in simulations.

where the variables appearing on the right-hand sides are dimensionless variables and those on the left-hand sides are the corresponding dimensional variables. Here v_A is the Alfvén velocity and μ_0 is the permeability of vacuum.

In the present work we consider an equilibrium profile of a currentless stellarator/heliotron plasma, for which the initial conditions for Eqs. (1)–(5) are given by $p = p_0(r)$ and $\phi = A = 0$. To model the stellarator/heliotron field of the system, we specify a functional form for $\iota(r)$ and then determine $\psi_h(r)$ and $\Omega(r)$ consistently through Eqs. (6) and (7). For boundary conditions, we assume the plasma is enclosed by a perfectly conductive wall and set $\omega(r=a)=0$, $\phi(r=a)=0$, $A(r=a)=0$, and $p(r=a)=0$ if no VMI exists.
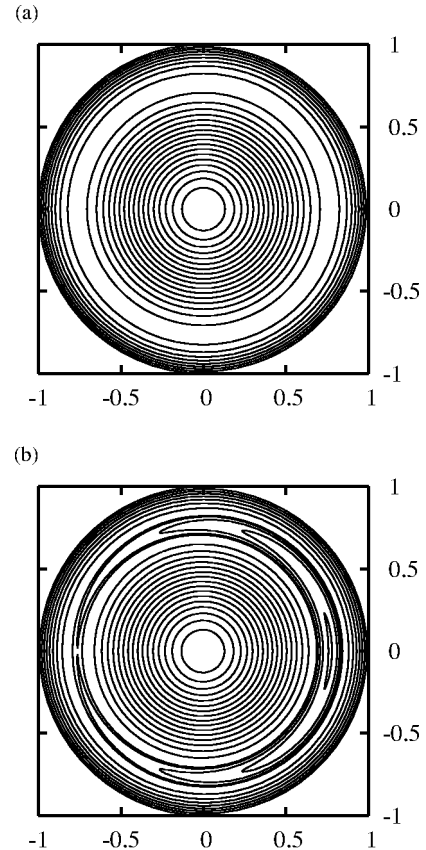
(a)

(b)

FIG. 4. Contour plots of the vacuum helical flux $\Psi_H^{(1,1)}$ with (a) $\psi_B = 1.0 \times 10^{-8}$ and (b) $\psi_B = 1.0 \times 10^{-3}$.
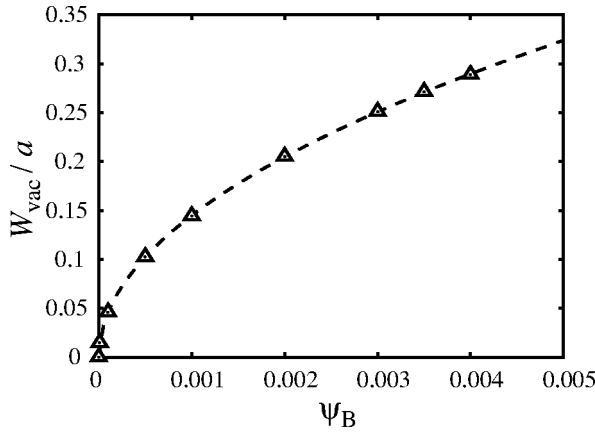
FIG. 5. The normalized width of the VMI, W_{vac}/a, as a function of ψ_B. The triangles denote data obtained from the simulation code and the broken line is a reference line that represents a function proportional to $\psi_B^{1/2}$.
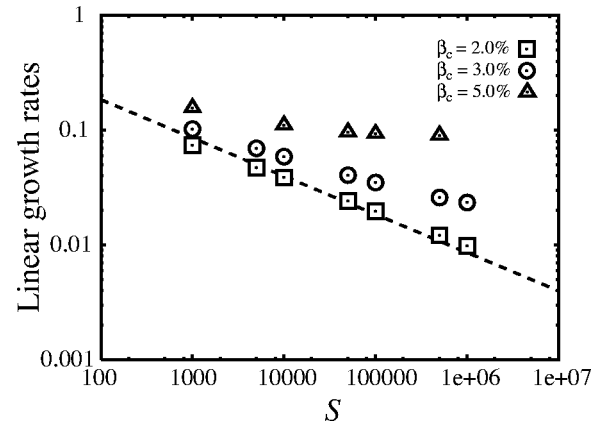

FIG. 6. The most unstable linear growth rates obtained from the time-dependent simulation code as functions of the magnetic Reynolds number S for $\beta_c = 2.0\%$, 3.0%, and 5.0%. The broken line represents a function proportional to $S^{-1/3}$ for reference.

When we apply external magnetic perturbations (in addition to the stellarator/heliotron field ψ_h) to generate VMIs, we set $A(r=a) = \psi_B \cos(m\theta+n\zeta)$ to emulate the field of magnetic perturbation coils at the boundary, where ψ_B is a constant and the integer pair (m,n) indicates the poloidal and toroidal mode numbers of the field.

The initial-boundary value problems for Eqs. (1)–(5) are solved numerically with the use of the FEM in the poloidal cross section and Fourier expansion in the ζ direction. The FEM grids consist of both quadrangle elements and triangle elements, as shown in Fig. 1. We use the conjugate gradient method with incomplete Cholesky preconditioner (i.e., ICCG method) to invert the matrix obtained from the finite element discretization. Details of the simulation algorithms will be published elsewhere.

III. SIMULATION PARAMETERS

The rotational transform used in the simulations presented here is given in Fig. 2. The aspect ratio is assumed to be $\epsilon = 6.25$, the pitch number $N = 10$, and the pole number $l = 2$. These machine parameters are the same as those of the LHD. Other parameters are: magnetic Reynolds number $S(\equiv 1/\eta_\parallel) = 1.0\times10^5$, viscosity $\mu = 5.0\times10^{-5}$, perpendicular thermal diffusivity $\chi_\perp = 1.0\times10^{-5}$ for modes with $n\neq0$ and $\chi_\perp = 1.0\times10^{-10}$ for the $n=0$ mode, and parallel thermal diffusivity $\chi_\parallel = 5.0\times10^{-3}$. The equilibrium pressure profile $p(r)$ is given in Fig. 3, where the pressure is assumed to be constant [i.e., $p(r)=p_0$] for $0<r<0.5$ and monotonically vary as $p_0(1-4(r-0.5)^2)^2$ for $0.5\leqslant r\leqslant1$. The beta value at the center $\beta_c = p_0/(B_0^2/2\mu_0)$ is set to be 2.0% unless otherwise indicated. The equilibrium given above is unstable to the resistive pressure driven mode. Thirteen toroidal modes from $n=0$ to $n=12$ are included in our nonlinear simulations.

As mentioned in Sec. II, we use the boundary condition $A(r=a) = \psi_B \cos(m\theta+n\zeta)$ to introduce a VMI. In order to control the $(m,n)=(1,1)$ island in the plasma, we set $(m,n)=(1,1)$ for this boundary condition. The total vacuum fields are plotted in Fig. 4, where the helical magnetic flux with $(m,n)=(1,1)$ helicity is defined as $\Psi_H^{(1,1)}(r,\theta,\zeta)$

$\equiv -r^2/2 - \psi^{(1,1)}(r,\theta,\zeta)$ with $\psi^{(1,1)}$ being the $(m,n)=(1,1)$ component of the total poloidal flux $\psi = A + \psi_h$. Here the poloidal flux A is obtained from the vacuum magnetic flux equation

$$\nabla^2 A = 0,$$

with the boundary condition $A(r=a) = \psi_B \cos(\theta+\zeta)$, as mentioned above. In Fig. 4(a), where $\psi_B = 1.0\times10^{-8}$, the perturbation modifies the initial concentric flux profile but no VMI is seen. In Fig. 4(b), where $\psi_B = 1.0\times10^{-3}$, a VMI of $(m,n)=(1,1)$ helicity is clearly seen. In this way, we can control the size of vacuum magnetic island by adjusting the parameter ψ_B. As shown in Fig. 5, the width of the VMI is proportional to $\psi_B^{1/2}$.

IV. SIMULATION RESULTS

We first check linear stability of the unperturbed system, i.e., system without a VMI (i.e., $\psi_B=0$). Figure 6 shows the linear growth rate obtained from time-evolution simulation of the linearized version of Eqs. (1)–(5) as a function of the magnetic Reynolds number S. In the case of $\beta_c=2.0\%$, the linear growth rate of the most unstable mode is proportional to $S^{-1/3}$, which indicates the instability is the resistive inter-
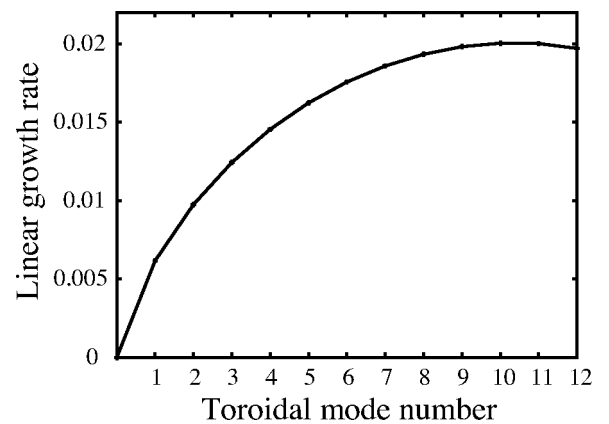

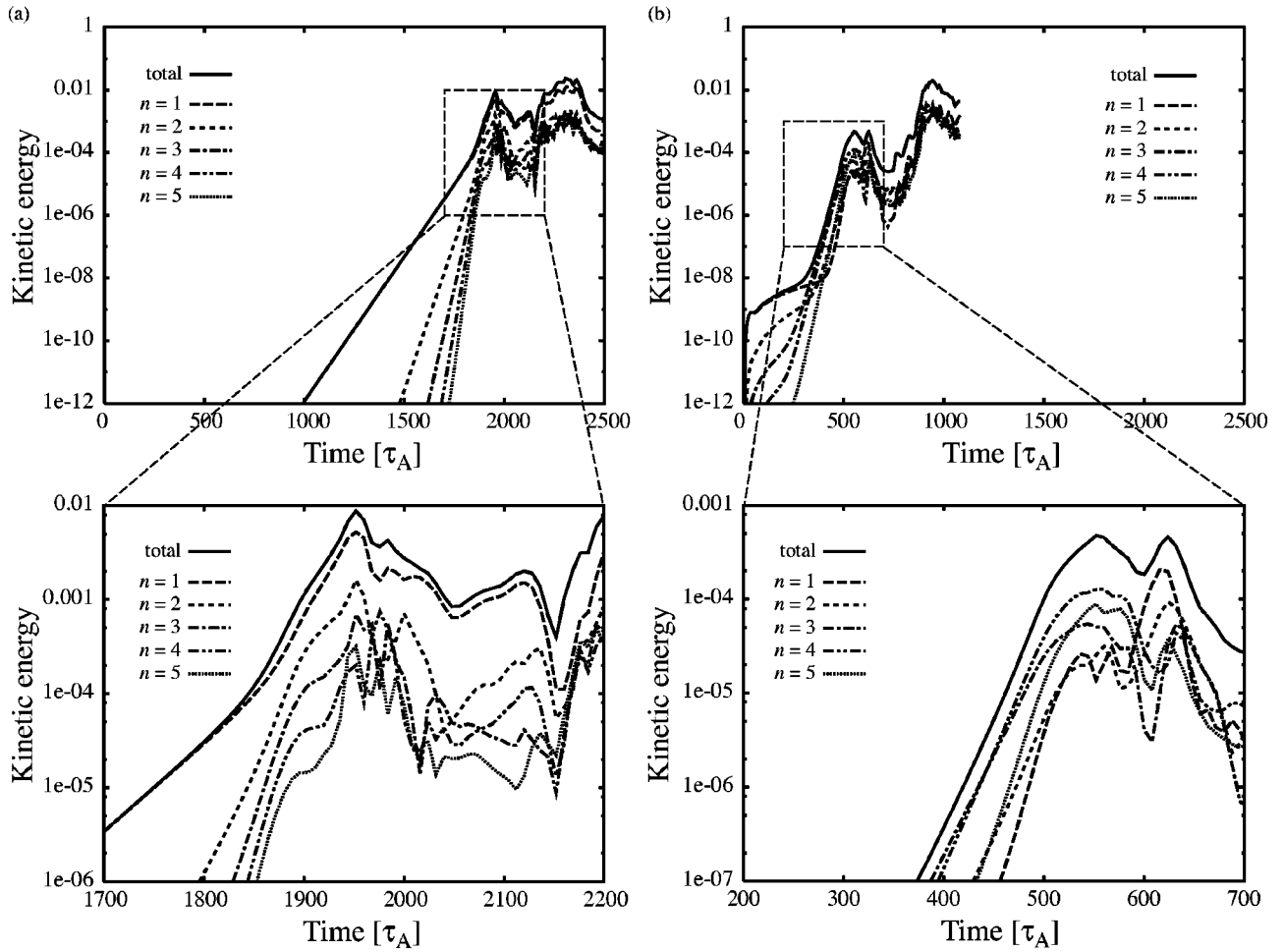FIG. 7. The linear growth rate as a function of the toroidal mode number n.

FIG. 8. Time evolution of the kinetic energy for each toroidal (i.e., n) mode for (a) $\psi_B = 1.0 \times 10^{-8}$ and (b) $\psi_B = 1.0 \times 10^{-3}$.

change mode. Figure 7 shows the linear growth rate as a function of the toroidal mode number n. It is seen that the linear growth rate has a peak at $n = 10$. It should be noted that the $n = 1$ mode also has a finite growth rate, which indicates that a VMI of $(m,n) = (1,1)$ helicity can trigger the growth of $n = 1$ mode.

For nonlinear simulations, we include finite VMIs, i.e., nonzero ψ_B. Nonlinear time evolution of the kinetic energy of each toroidal mode is shown in Figs. 8(a) and 8(b), where we set $\psi_B = 1.0 \times 10^{-8}$ [i.e., with no visible VMI as in Fig. 4(a)] for Fig. 8(a) and $\psi_B = 1.0 \times 10^{-3}$ [i.e., with a VMI whose width is 14% of the minor radius, as in Fig. 4(b)] for Fig. 8(b). Note that since a nonzero VMI serves as an initial perturbation to the $(m,n) = (1,1)$ mode, the (1, 1) mode may dominate in the early stage of nonlinear evolution despite the fact that the $n = 10$ mode has the largest growth rate. It is seen in Fig. 8(a) that the unstable modes saturate at $t \simeq 1950$, when the spectrum analysis of Fig. 9(a) indicates that the unstable modes are of $n/m = 1$ [i.e., $(m,n) = (1,1),(2,2),(3,3),\dots$]. Since the $n = 1$ mode is seen to have the largest magnitude in Fig. 8(a), the dominant mode at saturation is $(m,n) = (1,1)$. After saturation, the $n/m = 1$ modes start to decay. Subsequently other modes such as $n/m = 1/2, 2/3, 3/4, \dots$ become unstable, as shown in Fig. 9(b) and the total kinetic energy increases after $t \simeq 2160$

again. This is because the pressure profile modified by the $n/m = 1$ modes are steep on both sides of the $n/m = 1$ mode resonant surface, which drives other modes unstable [as shown in Fig. 13(a), which will be discussed later].

In Fig. 8(b), where we apply a stronger external perturbation field with $\psi_B = 1.0 \times 10^{-3}$, the resistive pressure driven mode appears to grow faster than in the case of Fig. 8(a). Furthermore, the initially dominant $n = 1$ mode, together with other modes, saturates at $t \simeq 500$ with the saturation level lower than that in Fig. 8(a) by two orders of magnitude. The dominant mode at saturation is seen to be $n = 4$, which is in contrast with the case of Fig. 8(a), where the $n = 1$ mode still dominates in the saturation phase. Figure 10(a) shows that the $n/m = 1$ mode is dominant at $t \simeq 500$ in Fig. 8(b), which indicates that the dominant mode at saturation is $(m,n) = (4,4)$. After saturation, $n/m \neq 1$ modes become unstable, as shown in Fig. 10(b).

The widths of magnetic islands generated by plasma instabilities are affected by the external magnetic perturbation. Figure 11 shows contour plots of the helical fluxes $\Psi_H^{(1,1)}$ at saturation for (a) $\psi_B = 1.0 \times 10^{-8}$ and (b) $\psi_B = 1.0 \times 10^{-3}$. In Fig. 11(a), magnetic islands are shown to be generated by the resistive pressure driven instability and the maximum width of them is 24% of the minor radius. For larger ψ_B, the mag-
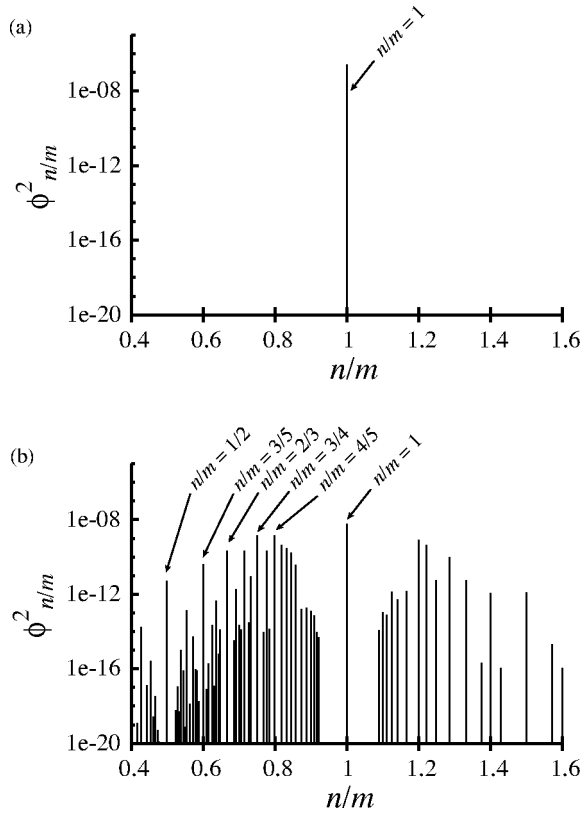
FIG. 9. Power spectra of the electrostatic potential functions ϕ of helicity n/m at (a) $t \simeq 1950$ and (b) $t \simeq 2160$ for the simulation given by Fig. 8(a).
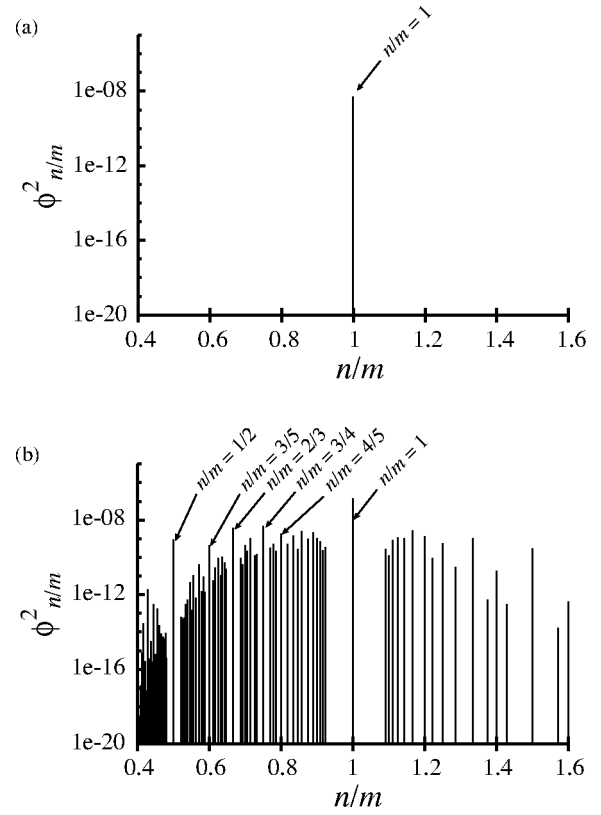

FIG. 10. Power spectra of the electrostatic potential functions ϕ of helicity n/m at (a) $t \simeq 550$ and (b) $t \simeq 900$ for the simulation given by Fig. 8(b).

netic perturbation forms a VMI as shown in Fig. 4(b) and its size seems to set a limit to the sizes of instability-induced magnetic islands. In Fig. 11(b), the maximum width of magnetic islands is 19% of the minor radius, i.e., essentially the size of the VMI. Furthermore, the envelope of magnetic islands in this case is similar in shape to that of the VMI given in Fig. 4(b).

Figure 12 shows the pressure profile in a poloidal cross section at saturation for (a) $\psi_B = 1.0 \times 10^{-8}$ and (b) $\psi_B = 1.0 \times 10^{-3}$. The pressure profile is more or less flattened at the radial location of the magnetic island. The region of the flat pressure profile is thinner when a VMI is present.

Figure 13 shows the time evolution of the average pressure [i.e., the $(m,n) = (0,0)$ component of the total pressure] for (a) $\psi_B = 1.0 \times 10^{-8}$ and (b) $\psi_B = 1.0 \times 10^{-3}$. In Fig. 13(a), the average pressure profile is shown to be nearly flat in the vicinity of the $n/m = 1$ mode resonant surface at $t \simeq 1950$. This change of the pressure profile simultaneously makes pressure gradients steeper on both sides of the mode resonant surface, causing $n/m \neq 1$ modes to grow rapidly after $t \simeq 2160$. The series of excited instabilities with different helicities change the average pressure profile over a wide range rapidly after $t \simeq 2200$. In Fig. 13(b) the pressure gradient is also shown to become more or less flat in the vicinity of the $n/m = 1$ mode resonant surface. However, due to the presence of a VMI, the width of the flat pressure region is narrow for a longer period in this case. It follows that the growth of $n/m \neq 1$ modes are also slower than in the case of Fig. 13(a).

Correlations between the widths of the actual magnetic

island W in the plasma as well as the flat pressure region W_{prs} at saturation and the width of the VMI W_{vac} are given in Fig. 14. A circle denotes the correlation between W and W_{vac} and a triangle denotes that between W_{prs} and W_{vac}. The island widths W and W_{prs} are evaluated during the time period when the widths are well defined and nearly constant (as can be seen in Fig. 13), i.e., after the $n/m = 1$ modes saturate and while the dominant components remain to be $n/m = 1$ (i.e., before $n/m \neq 1$ modes grow significantly). We carefully selected such time periods by observing the time evolution of kinetic energy and analyzing its spectra, as those given in Figs. 8–10. In the absence of a VMI, the width of the magnetic island in the plasma W is about 24% of the minor radius. As we increase W_{vac} from null, W decreases until both the magnetic island in the plasma and the VMI approximately have the same width, i.e., about 15%–20% of the minor radius. For larger W_{vac}, W becomes essentially the same as W_{vac}. Similarly the width of the flat pressure region W_{prs} decreases as W_{vac} increases from null. However W_{prs} remains small (about 5% of the minor radius) after W_{vac} becomes almost equal to W_{prs}. We believe this difference in W_{vac} dependence between W and W_{prs} is caused by the small parallel thermal diffusivity $\chi_\parallel$ employed here. (We used a relatively small value for $\chi_\parallel$, i.e., $\chi_\parallel = 5.0 \times 10^{-3}$, in order to achieve numerical stability.) With more realistic $\chi_\parallel$ [i.e., $\chi_\parallel \sim \mathcal{O}(1)$], we expect W_{prs} increases as W_{vac} increases after W_{vac} surpasses W_{prs} due to fast thermalization along the field lines. Effects of realistic $\chi_\parallel$ will be examined in future work. Simulations with slightly smaller β_c ($= 1.8\%$) are also
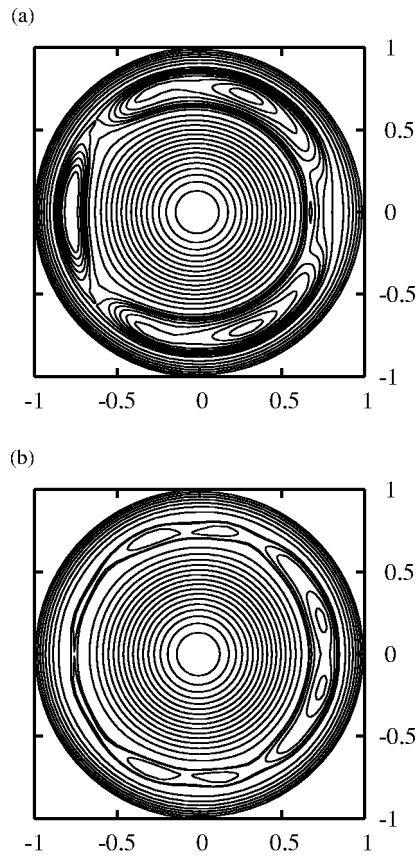
(a)

(b)

FIG. 11. Contour plots of the total helical flux $\Psi_H^{(1,1)}$ at saturation (a) at $t = 2020$ with $\psi_B = 1.0 \times 10^{-8}$ and (b) at $t = 700$ with $\psi_B = 1.0 \times 10^{-3}$.

carried out and a similar tendency is observed, as shown in Fig. 15.

V. SUMMARY

Using nonlinear numerical simulations, we have examined mechanisms of controlling magnetic islands in a stellarator/heliotron plasma by externally applying magnetic field perturbations that can generate a VMI. The simulation code we have developed and used for this study solves time-dependent nonlinear RMHD equations in a cylindrical geom-
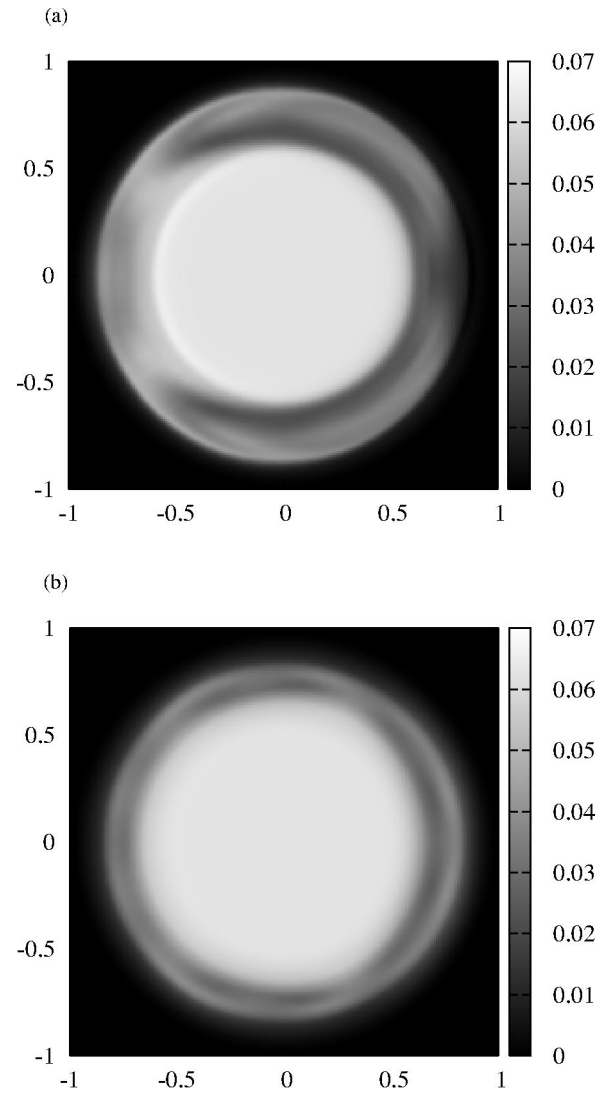
(a)

(b)

FIG. 12. Contour plots of plasma pressures (a) at $t = 2020$ for $\psi_B = 1.0 \times 10^{-8}$ and (b) at $t = 700$ for $\psi_B = 1.0 \times 10^{-3}$.

etry and is based on the FEM in the poloidal cross section and Fourier expansion in the longitudinal direction. It is demonstrated that the saturation width of a magnetic island in a plasma generated by resistive pressure-driven instabili-
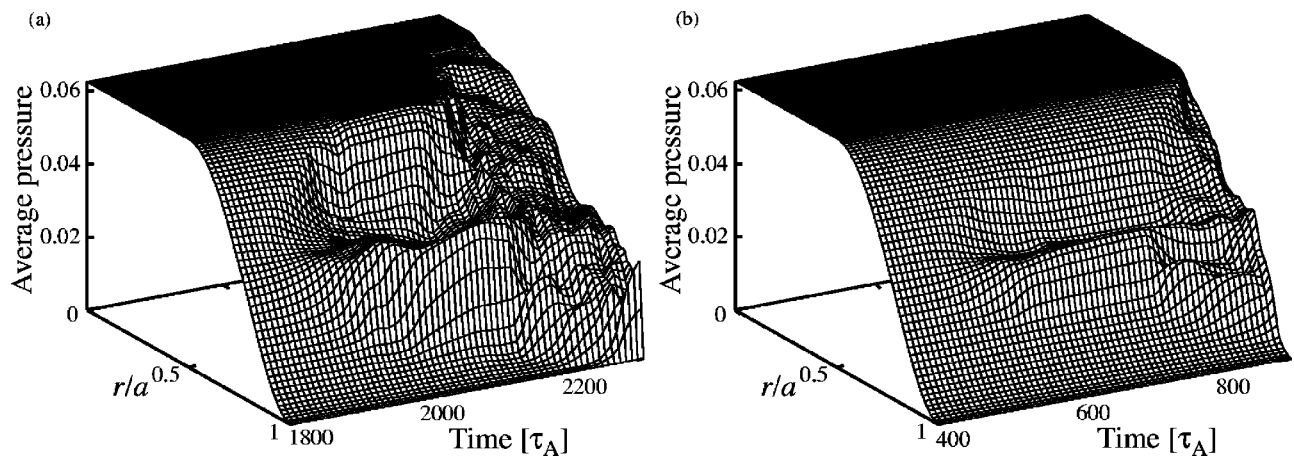
(a)

(b)

FIG. 13. Time evolution of the average pressure profile for (a) $\psi_B = 1.0 \times 10^{-8}$ and (b) $\psi = 1.0 \times 10^{-3}$.
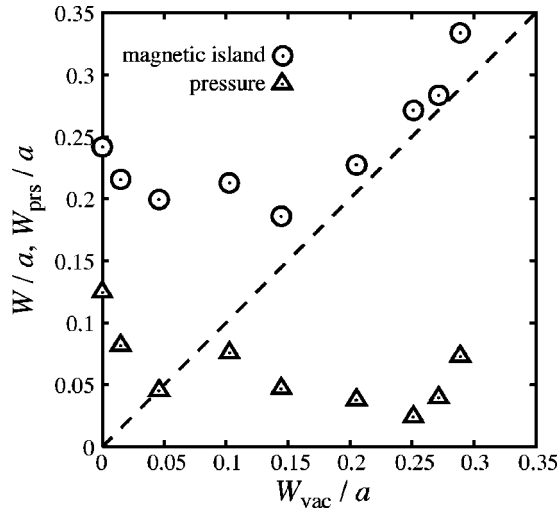
FIG. 14. The widths of the magnetic island W and flat pressure region W_{prs} as functions of the width of the VMI W_{vac}. All parameters are the same as those in the previous figures ($\beta_c = 2.0\%$).

ties can be controlled by a VMI generated by external perturbation coil systems.

As can be seen at the early stage of mode evolution in Figs. 8(a) and 8(b), in the presence of a VMI field, high n modes exhibit higher growth rates than low n modes and, at saturation, the $n=4$ mode dominates under the conditions given in Fig. 8(b). This contrasts with the case of a weak external perturbation (i.e., no VMI) given in Fig. 8(a), where the dominant mode at saturation is the $n=1$ mode. We also
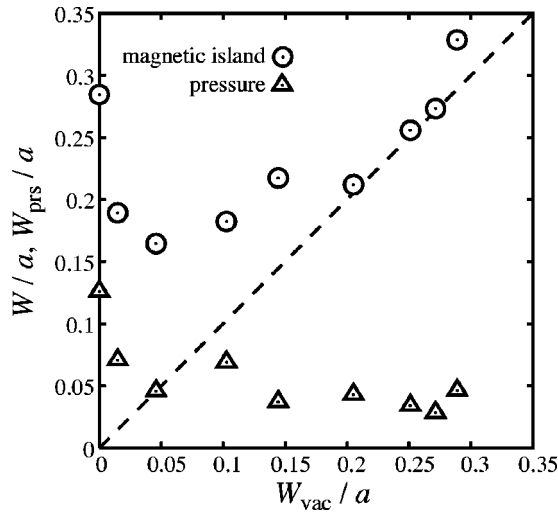

FIG. 15. The widths of the magnetic island W and flat pressure region W_{prs} as functions of the width of the VMI. All parameters are the same as those in Fig. 14 except $\beta_c = 1.8\%$.

note that the perturbation energy level during island saturation (i.e., when well-defined $n/m=1$ islands are formed) in Fig. 8(b) is significantly lower (by two orders of magnitude) than that in Fig. 8(a).

Since the structures of high (m,n) modes are more localized radially than those of low (m,n) modes, we expect that the flat pressure regions caused by nonlinear mode saturation of high (m,n) modes are also narrower than those caused by low (m,n) modes. Furthermore, for the same reason, relatively low amplitudes are required for high (m,n) modes to nonlinearly produce the $(m,n)=(0,0)$ pressure component that cancels the local pressure gradient. This explains the low saturation level observed in Fig. 8(b). This local flattening of pressure also reduces the growth rates and saturation levels of low (m,n) modes with $n/m=1$ [such as $(1,1)$ and $(2,2)$ modes]. In other words, the presence of an $(m,n)=(1,1)$ VMI can significantly lower the saturation levels of $n/m=1$ resistive interchange modes.

As shown in Fig. 13(a), if a nonlinearly formed flat pressure region is wide, the pressure gradients adjacent to it become large, which can destabilize $n/m \neq 1$ modes and deteriorate the entire plasma. On the other hand, as in the case of Fig. 13(b), if a flat pressure region is narrow, the pressure gradients adjacent to it do not become too steep and therefore the plasma is generally more stable.

Our three-dimensional simulations have thus demonstrated that if an $(m,n)=(1,1)$ VMI is applied to a stellarator/heliotron plasma, the plasma can develop resistance to the growth of magnetic islands arising from nonlinear resistive pressure driven modes. Especially, as shown in Figs. 14 and 15, the saturation width of an instability-induced magnetic island decreases as the external perturbation field increases until the size of the VMI takes over that of the instability-induced magnetic island.

[1] S. Hamaguchi, Phys. Fluids B **1**, 1416 (1989).
[2] K. Nishikawa and M. Wakatani, *Plasma Physics: Basic Theory with Fusion Applications*, 3rd ed. (Springer, New York, 1999), p. 205.
[3] P. Furth, J. Killeen, and M. N. Rosenbluth, Phys. Fluids **6**, 459 (1963).
[4] A. Iiyoshi, M. Fujiwara, O. Motojima, N. Ohyabu, and K. Yamazaki, Fusion Technol. **17**, 169 (1990).
[5] H. Yamada, A. Komori, N. Ohyabu *et al.*, Plasma Phys. Controlled Fusion **43**, A55 (2001).
[6] T. Tatsuno, M. Wakatani, and K. Ichiguchi, Nucl. Fusion **39**, 1391 (1999).
[7] B. A. Carreras, V. E. Lynch, K. Ichiguchi, T. Tatsuno, and M. Wakatani, Plasma Phys. Rep. **25**, 958 (1999).
[8] K. Ichiguchi, M. Wakatani, T. Unemura, T. Tatsuno, and B. A. Carreras, Nucl. Fusion **41**, 181 (2001).
[9] B. A. Carreras, V. E. Lynch, K. Ichiguchi, M. Wakatani, and T. Tatsuno, Phys. Plasmas **8**, 990 (2001).
[10] K. Ida, N. Ohyabu, T. Morisaki *et al.*, Phys. Rev. Lett. **88**, 015002 (2002).
[11] N. Ohyabu, K. Ida, T. Morisaki *et al.*, Phys. Rev. Lett. **88**, 055005 (2002).
[12] M. Wakatani, Nucl. Fusion **18**, 1499 (1978).
[13] H. R. Strauss, Plasma Phys. **22**, 733 (1980).
[14] M. Wakatani, *Stellarator and Heliotron Devices* (Oxford University Press, New York, 1998), p. 98.